

UKAEA-CCFE-PR(20)116

G. M. Staebler, J. Candy, E. Belli, J. E. Kinsey, N.
Bonanomi, B. Patel

Geometry dependence of the fluctuation intensity in gyrokinetic turbulence

Enquiries about copyright and reproduction should in the first instance be addressed to the UKAEA Publications Officer, Culham Science Centre, Building K1/O/83 Abingdon, Oxfordshire, OX14 3DB, UK. The United Kingdom Atomic Energy Authority is the copyright holder.

The contents of this document and all other UKAEA Preprints, Reports and Conference Papers are available to view online free at scientific-publications.ukaea.uk/

Geometry dependence of the fluctuation intensity in gyrokinetic turbulence

G. M. Staebler, J. Candy, E. Belli, J. E. Kinsey, N. Bonanomi, B.
Patel

Geometry dependence of the fluctuation intensity in gyrokinetic turbulence

G. M. Staebler¹, J. Candy¹, E. Belli¹, J. E. Kinsey²,
N. Bonanomi³, and B. Patel^{4,5}

¹General Atomics, San Diego, USA

²CompX, San Diego, USA

³IPP, Garching, Germany

⁴CCFE, Culham, UK

⁵York Plasma Institute, University of York, UK

E-mail: Gary.Staebler@gat.com

Abstract. The findings of an investigation into the properties of the three dimensional (3D) saturated fluctuation intensity of the electric potential in gyrokinetic turbulence simulations is presented. Scans in flux surface elongation and Shafranov shift are used to isolate the tokamak geometric dependencies. The potential intensity required in order to compute exact fluxes by a quasilinear method is determined using linear eigenmodes computed with the gyrokinetic code. A model of this non-linear intensity is constructed using the linear eigenmode properties and the geometry shape functions obtained from the 3D intensity spectrum. The model computes the poloidal wavenumber spectrum of the electron and ion energy fluxes with unprecedented accuracy. New insights are gained into the way zonal flow mixing saturates ion-scale turbulence by controlling the radial wavenumber width of the turbulence spectrum.

Submitted to: *Plasma Phys. Control. Fusion*

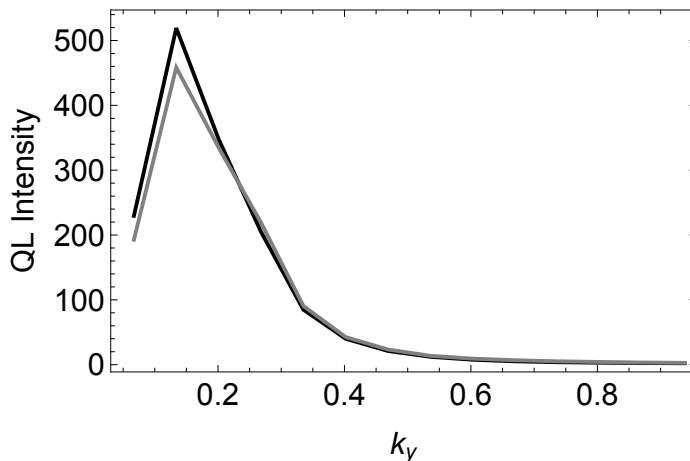


Figure 1. The QL intensity computed from the ion (black) and electron (gray) energy flux for the GA-STD case

1. Introduction

Gaining an empirical understanding of turbulence by examining the properties of the spectra is not as daunting a task as it might seem. The goal is not to understand everything about the temporal and spatial behaviour of the turbulence. The goal of this study is just to model the electric potential (time dependent electrostatic potential) intensity required to compute the fluxes using the quasi-linear approximation (QL intensity) [1]. To be specific, the intensity of each poloidal wavenumber (k_y) required is the non-linear contribution to that wavenumber (Q_{k_y}) divided by the quasilinear weight of the most unstable linear eigenmode ($W_{k_y}^{QL}$) and the wavenumber spacing dk_y .

$$I_{k_y}^{QL} = \frac{Q_{ak_y}}{dk_y W_{ak_y}^{QL}} \quad (1)$$

The quasi-linear weight is the formula for the non-linear flux (Eq. 2) evaluated with just the most unstable linear eigenmode wavefunction (times a delta-function in k_x and k_y) and divided by the square amplitude (intensity) of the electric potential of that linear mode. The poloidal wavenumber grid interval dk_y is needed in Eq. 1 to make the intensity independent of the k_y grid. It should not matter which plasma species (subscript label "a") is used to compute this intensity, since the species dependence is accounted for in the quasi-linear weight. This is illustrated in Fig. 1 with an example from one of the simulations discussed later. All of the cases were found to give good agreement between the electron and ion calculations of the QL intensity. Using the same code to compute the linear eigenmodes, and the non-linear turbulence driven fluxes, eliminates the error due to approximated linear eigenmodes used in quasi-linear transport models like TGLF [2]. The saturation models used in TGLF prior to this paper were constructed based on the flux surface average potential intensity at $k_x = 0$,

not the QL intensity as defined in Eq. 1. The turbulent energy flux in the gyrokinetic simulation is computed for each species by the formula

$$Q_a = \sum_{k_x} \sum_{k_y} \frac{3}{2} \langle \text{Re} [i k_y \frac{a e \tilde{\phi}_{k_x, k_y}^*}{\rho_s T_e} \frac{a \tilde{p}_{a, k_x, k_y}}{\rho_s n_e T_e}] \rangle_{t, \theta} = \sum_{k_y} Q_{a k_y} \quad (2)$$

Here the gyro-Bohm normalizations of the CGYRO code were used [3]: $c_s = \sqrt{T_e/m_D}$, $a =$ minor radius at separatrix, $\rho_s = c_s/\Omega_s$, $\Omega_s = eB_{\text{unit}}/(m_D c)$, $B_{\text{unit}} = \frac{qd\psi}{rdr}$ [4] for poloidal magnetic flux ψ , and $m_D =$ deuterium mass. The gyro-Bohm normalization for energy flux in these units is $n_e T_e c_s (\rho_s/a)^2$. The energy flux is produced by a radial $E \times B$ drift driven by electric potential fluctuations $\tilde{\phi}_{k_x, k_y}$ that is averaged with the fluctuations of the pressure moment of the species distribution function (\tilde{p}_{a, k_x, k_y}). The angle bracket represents a time average (t) and a flux surface average over a poloidal angle (θ). There is also a sum over the normalized radial wavenumber (k_x) which is equivalent to a radial average over the flux tube box. In this paper, we will be examining how the radial wavenumber and poloidal dependence of the time average electric potential intensity influence the QL intensity. Insights into the geometry dependence and the way in which the zonal ($k_y = 0$) potential fluctuations control the radial wavenumber width of the whole spectrum will be gained. A model for the QL intensity of unprecedented accuracy is constructed using these new results. This new model (SAT2) improves the ion-scale part of the model (SAT1) [5] that was developed to fit coupled electron-ion multi-scale gyrokinetic simulation spectra [6].

In section 2 the geometric metrics that make the wavevector coordinate independent and how these could impact the geometry dependence of the intensity will be discussed. In section 3 the intensity spectrum at the outboard midplane will be used to study the radial wavenumber width and its relation to the zonal potential fluctuations. In section 4 the poloidal dependence of the 3D spectrum will be studied. It will be shown that the wavenumber metrics can account for the poloidal dependence of the peak of the spectrum at $k_x = 0$. In section 5 a model for the QL intensity will be fit incorporating the radial wavenumber spectral width and flux surface average of the poloidally varying factors. The final section summarizes the paper and discusses the potential impact of this new SAT2 model on transport modeling of tokamaks and spherical tori.

2. Wavevector metrics in axisymmetric geometry

The geometric metrics that enter the gyrokinetic equation for general, axisymmetric, closed flux surface geometry will be shown in this paper to provide the functions that fit the poloidal dependence of the saturated potential intensity. The gyrokinetic equation is an approximation to the Vlasov-Fokker-Planck equation based on an expansion in the ratio of the magnetic gyroradius (Larmor radius) to the local equilibrium gradient length. This is a very small parameter in tokamaks and

spherical torii with magnetic fields greater than one Tesla typical of today's fusion energy experiments. Because the gyroradius sets the scale for the plasma turbulence described by gyrokinetics, the wavelength perpendicular to the magnetic field is much shorter than the wavelength parallel to the magnetic field. This property makes it convenient to introduce an eikonal approximation for the perpendicular wavevector. The gradient of the eikonal (S) is perpendicular to the magnetic field vector \mathbf{B} : $\mathbf{B} \cdot \nabla S = 0$. There are two independent functions that satisfy this constraint. An arbitrary function of the poloidal flux $S = S_x(\psi)$ and $S = n[\varphi + S_y]$ where n is a toroidal mode index and

$$S_y = - \int_0^\theta d\theta' \frac{B_T}{R \mathbf{B}_p \cdot \nabla \theta'} \quad (3)$$

Here a cylindrical coordinate system (R, φ, Z) is assumed and the magnetic field has toroidal $\mathbf{B}_T = I_T(\psi) \nabla \varphi$ and poloidal $\mathbf{B}_p = \nabla \varphi \times \nabla \psi$ components. The Miller geometry coordinates [7], minor radius and poloidal angle (r, θ) , have been used for S_y . The eikonal function S_y is quasi-periodic with $S_y(\theta = 2\pi) = 2\pi q$ where q is the safety factor of the flux surface. An average over the fast motion about the magnetic field is taken in the gyrokinetic approximation. This results in Bessel functions with an argument $|\nabla S| v_\perp m_a c / (Z_a B)$. This motivates defining a poloidally varying wavevector given by

$$K_\perp^2 = \rho_B^2 |\nabla S|^2 = \left[K_y^2 + \left(\hat{s} K_y \Theta + K_x \right)^2 \right] \quad (4)$$

Where $\rho_B = \sqrt{T_e/m_D}/\Omega_B$, $\Omega_B = \frac{eB}{m_D c}$ are a gyro-radius and gyro-frequency using the CGYRO units [3] of temperature and mass (T_e, m_D) but using the total magnetic field magnitude $B(\theta)$. The magnetic shear is $\hat{s} = (r/q) dq/dr$. The generalized angle Θ in Eq. 4 is defined to be zero at the outboard midplane and has a quasi-periodic property derived from S_y . The poloidal K_y and radial K_x wavenumber components in Eq. 4 are defined by

$$K_y(\theta) = \frac{n \rho_{B_p}}{R} = \frac{k_y}{|\nabla r|} \quad (5)$$

$$K_x(\theta) = |\nabla r| k_r \rho_B = \frac{k_x}{G_q} \frac{B_{\text{norm}}}{B_{\text{unit}}} \quad (6)$$

where the flux surface shape factor G_q has been introduced to make the distinction between the arbitrary normalizing magnetic field B_{norm} and B_{unit} , which appears in the metric coefficients, clear.

$$G_q = \frac{rB}{qRB_p} = \frac{B}{B_{\text{unit}} |\nabla r|} \quad (7)$$

This shape factor reduces to 1 for a large aspect ratio circular flux surface. It is the same for GENE or CGYRO since it does not involve the choice of normalizing magnetic field. The poloidal wavenumber K_y (Eq. 5) is the toroidal wavenumber n/R normalized by the gyroradius with respect to the poloidal magnetic field $\rho_{B_p} = \rho_B B/B_p$. The radial wavenumber K_x (Eq. 6) is the gradient normal to flux surfaces ($|\nabla r| k_r = |\nabla S_x|$)

normalized to the the total magnetic field gyro-radius. The relation of these geometric wavenumbers to the standard normalized wavevectors k_y , and $k_x = k_r \rho_{B_{\text{norm}}}$ is also given in Eq. 5,6. The CGYRO code uses the normalizing magnetic field $B_{\text{norm}} = B_{\text{unit}}$. The GENE code [8] uses the same poloidal wavenumber k_y as CGYRO, but the normalizing magnetic field is $B_{\text{norm}} = B_{\text{ref}}$ [9] (the toroidal magnetic field at the magnetic axis). There can also be differences in the reference temperature and mass compared to what is used here (T_e , m_D) for the gyrokinetic codes but these are taken to be the same for both codes. The two sources for the poloidal angular dependence of the wavevector are the magnetic field strength (B) and the gradient of the minor radius $|\nabla r|$ (equivalent to $|\nabla\psi| = RB_p$).

We seek to build a model, using the linear CGYRO eigenmode spectrum, for the normalized amplitude of the 3D potential fluctuations

$$\Phi(k_y, k_x, \theta) = \frac{e|\tilde{\phi}|}{T_e \sqrt{dk_y dk_x} \rho_{B_{\text{norm}}}} \frac{a}{\rho_{B_{\text{norm}}}} \quad (8)$$

The factor $\sqrt{dk_y dk_x}$ in Eq. 8 is needed in order to make the intensity independent of the spacing between the wavenumbers dk_y and dk_x . For the zonal potential ($k_y = 0$) the dk_y is set to 1 in Eq. 8. The model for the peak of the potential amplitude is chosen to have the mode-coupling saturation form [5].

$$\Phi_{k_y}^{\text{model}} = \frac{\gamma_{k_y}^{\text{eff}}}{k_x^{\text{RMS}} k_y} \quad (9)$$

The primary goal of this paper is to determine the geometric factors required to generalize this model to be θ dependent. The model is exact if the effective growthrate $\gamma_{k_y}^{\text{eff}}$ and the root mean squared (RMS) width of the radial wavenumber spectrum k_x^{RMS} are computed from the non-linear spectrum.

$$k_x^{\text{RMS}} = \sqrt{\frac{\sum_{k_x} k_x^2 \Phi^2(k_x, k_y, \theta)}{\sum_{k_x} \Phi^2(k_x, k_y, \theta)}} \quad (10)$$

$$\gamma_{k_y}^{\text{eff}} = k_x^{\text{RMS}} k_y \Phi(k_x = 0, k_y, \theta) \quad (11)$$

The model for the QL intensity is the flux surface average of the square of the peak amplitude

$$I_{k_y}^{\text{model}} = \left\langle \left(\Phi_{k_y}^{\text{model}} \right)^2 \right\rangle_{\theta} \quad (12)$$

Note that this model has a simple transformation to the general geometry wavenumbers by changing the normalization of the potential to ρ_B

$$\frac{\rho_{B_{\text{norm}}}}{\rho_B} \Phi_{k_y}^{\text{model}} = \frac{\gamma_{k_y}^{\text{eff}}}{K_x^{\text{RMS}} K_y} \quad (13)$$

The factor k_x^{RMS} in Eq. 9 and the use of the the $k_x = 0$ peak in the definition for $\gamma_{k_y}^{\text{eff}}$ (Eq. 11) makes the model Eq. 9 independent of k_x . This model form has been found [5] to give a better fit to the way the fluxes fall off with k_y than other ways of modeling the impact of the k_x average of the flux calculation (Eq. 2).

3. The role of the radial wavenumber spectrum width in turbulence saturation

In order to investigate the geometry dependence of the saturated potential intensity a set of gyrokinetic turbulence simulations were performed. A scan of the elongation of the flux surface (κ) changes the factor B/B_{unit} [4]. At the outboard midplane ($\theta = 0$) this factor scales like $1/\kappa$. The gradient of the minor radius at the outboard midplane is $\text{grad}r_0 = |\nabla r|_{\theta=0} = 1/(1 + \Delta)$ where $\Delta = dR_0/dr$ is the Shafranov shift of the major radius of the flux surface center (R_0). Starting with the GA-STD parameters ($a/L_n = 1$, $a/L_T = 3.0$, $q = 2.0$, $T_D/T_e = 1$, $\hat{s} = 1.0$, $\kappa = 1.0$, $\Delta = 0.0$), scans in $\kappa = (1.0, 1.25, 1.5, 1.75, 2.0)$ and $\Delta = (0.0, -0.1, -0.2, -0.4, -0.5)$ were run with CGYRO. A pure deuterium plasma, with a very low electron pressure ($\text{BETAE_UNIT} = 0.0005$), is assumed. For 7 of the cases the collision frequency of $\text{NU_EE} = \nu_{ee}a/c_s = 0.05$ was used. These cases had 24 positive poloidal wavenumbers with spacing $dk_y = 0.067$ and 144 positive radial wavenumbers with spacing $dk_x = 2\pi\hat{s}dk_y/N_{\text{box}}$ where $N_{\text{box}} = 6$ is the `BOX_SIZE` setting for CGYRO and $\hat{s} = 1$ is the magnetic shear. Another three cases were run with collision frequency $\text{NU_EE} = 0.1$ and $\Delta = 0, -0.5$, $\kappa = 2.0$ (16 $k'_y s$ with $dk_y = 0.067$, 129 $k'_x s$, $N_{\text{box}} = 13$). These three cases were also run with GENE (20 $k'_y s$ with $dk_y = 0.05$, 159 $k'_x s$, $N_{\text{box}} = 12$). One case was re-run with twice the value of dk_x in order to verify the scaling of the intensity with the radial wavenumber spacing. The 10 CGYRO cases were sufficient to deduce the dependence of the radial wavenumber width on the outboard midplane $|\nabla r|_0$ and $B(0)/B_{\text{unit}}$ as discussed in this section. The GENE runs were used to verify the dependence on the reference magnetic field. The other normalizations were the same for both gyrokinetic codes.

The physical picture of the saturation of the gyrokinetic turbulence by zonal flow mixing [5] is that the $k_y = 0$ zonal fluctuations (non-static part) couple the fastest growing $k_x = 0$ modes at each k_y to slower growing, or damped, modes at larger k_x . This coupling is through non-linear advection by the time dependent zonal fluctuations (not zonal flow shear). It was shown in Ref. [5] that this mechanism was able to contribute to the saturation of even electron gyroradius scale modes, since the zonal flow mixing rate $\gamma_{ZF} = V_{ZF}k_y$ is able to compete with the linear growthrate γ_{k_y} at all k_y scales. The zonal ExB fluctuation saturates when the zonal flow mixing rate is balanced by the linear growthrate of the mode being advected. This gives an approximate relation for the RMS zonal ExB velocity that can be computed from the linear eigenmode spectrum

$$V_{ZF} = \max[\gamma_{k_y}/k_y] \quad (14)$$

The growthrate is for the most unstable mode at each k_y . The RMS zonal flow velocity can be computed directly from the non-linear saturated spectrum

$$V_{ZF} = 0.5 \sqrt{\sum_{k_x} k_x^2 \Phi^2(k_x, k_y = 0, \theta)} \quad (15)$$

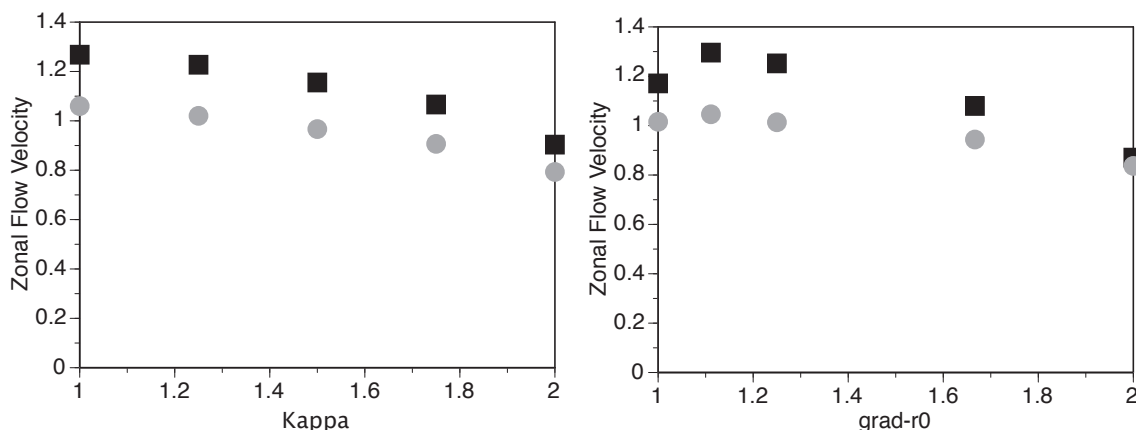


Figure 2. The zonal flow velocity computed from the potential spectrum Eq. 15 (black, box) and from the zonal flow mixing rule Eq. 14 (gray, circle) for elongation (κ) (left) and Shafranov shift (Δ) (right) scans. note: $\text{grad}r_0 = |\nabla r|_0 = 1/(1 + \Delta)$

The first test of the geometry dependence is to check the zonal flow (ZF) mixing rule (Eq. 14). The zonal flow velocity (Eq. 15) at $\theta = 0$ and the right hand side of the ZF mixing rule (Eq. 14) are plotted for the 10 cases in the κ and Δ scans in Fig. 2. The approximate ZF mixing rule Eq. 14 tracks the κ and Δ dependence pretty well. The factor of 0.5 is not optimal in Eq. 15. The variation in the zonal velocity is much smaller than the factor of two variation in $B(0)/B_{\text{unit}}$ or $|\nabla r|_0$ and does not require any geometric correction. Note that the zonal flow velocity (Eq. 15) is independent of the reference magnetic field since the gyroradius normalization of k_x and Φ cancel. The definition for V_{ZF} in Eq. 15 was changed from the original definition [5] to make this property obvious. It will be shown in the next section that the zonal potential is almost independent of the poloidal angle, so the ZF mixing rule holds approximately at all θ .

The RMS width of the k_x spectrum can be computed from Eq. 10 but this is not very accurate. The amplitude is well approximated by a Lorentzian function for moderate k_x/k_y but has a low amplitude tail at high k_x/k_y that makes using the formula Eq. 10 dependent on the range of k_x/k_y . To improve the calculation, a Lorentzian model was fit to the potential amplitude at the outboard midplane.

$$\Phi^{\text{fit}} = \frac{\Phi_0}{1 + \left(\frac{k_x}{k_{x\text{-width}}}\right)^2} \quad (16)$$

The two parameters Φ_0 and $k_{x\text{-width}}$ are determined by a least squares fit to a set of k_x points sampled from the potential. The impact of equilibrium $E \times B$ velocity shear can be easily added to this model [10]. Evaluating k_x^{RMS} (Eq. 10) with this Lorentzian model finds $k_x^{\text{RMS}} = k_{x\text{-width}}$. As shown in Fig. 3, the fit is very good for higher k_y but not as good for the zonal potential ($k_y = 0$). Note that the zonal potential at $k_x = 0$ is set to zero by the CGYRO code. The fit finder does not use this central point and it does not contribute to V_{ZF} . The whole k_y spectrum of the k_x^{RMS} for the GA-STD case is shown in Fig. 4 (left). It has a pronounced flatness at low- k_y and is basically linear in

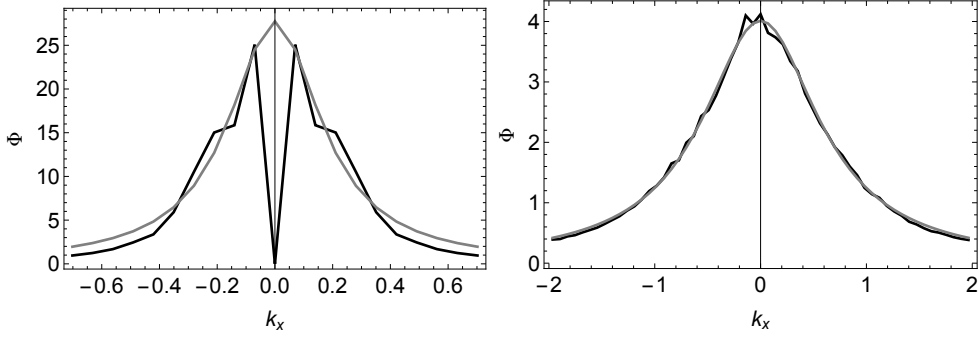


Figure 3. The normalized potential amplitude (Eq. 8) k_x -spectrum (black) and Lorentzian fit (gray) for (left) the zonal $k_y = 0$ and (right) finite $k_y = 0.603$ fits at the outboard midplane for the GA-STD case

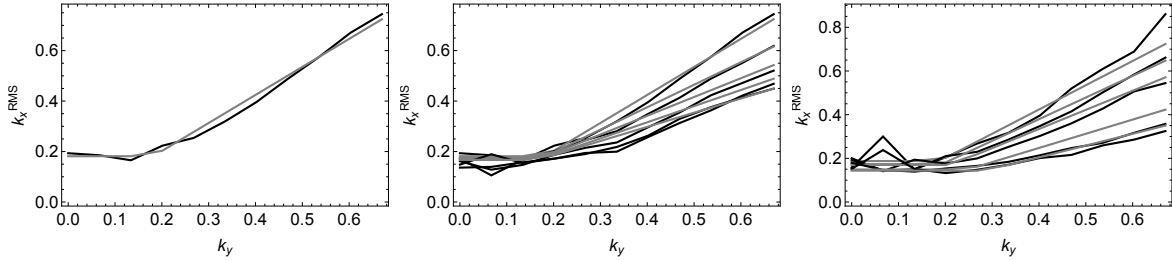


Figure 4. The k_x -width computed from the potential intensity at the outboard midplane (black) and the model (gray) (Eq. 17) for (left) GA-STD (center) κ scan and (right) Δ scan

k_y for higher values. A fit to this spectrum is shown in the figure given by the formula

$$\begin{aligned}
 k_x^{\text{model}} &= \frac{B_{\text{unit}}}{B_{\text{norm}}} k_{\text{ycut}} / |\nabla r|_0 \quad \text{for } k_y < k_{\text{ycut}} \\
 &= \frac{B_{\text{unit}}}{B_{\text{norm}}} \left(k_{\text{ycut}} / |\nabla r|_0 + b_1 (k_y - k_{\text{ycut}}) G_q(0) \right) \quad \text{for } k_y \geq k_{\text{ycut}}
 \end{aligned}
 \tag{17}$$

The cutoff is modeled by $k_{\text{ycut}} = b_0 k_{y\text{max}}$ where $k_{y\text{max}}$ is the value of k_y where γ_{k_y}/k_y is maximum. The two fitting coefficients used in Fig. 4 are $b_0 = 0.83$, $b_1 = 1.31$. The geometric coefficients in Eq. 17 were determined by the κ (center) and Δ (right) scans shown in Fig. 4. The change in slope and the nearly constant value of the width at $k_y=0$ are well fit by this model with the same coefficients. The oscillations at low- k_y suggest that there are slowly evolving contributions to the potential spectrum that have not been time averaged sufficiently. The GENE simulations are well fit by the same model (Eq. 17) verifying the overall B_{norm} factor.

The width of the zonal potential fluctuation amplitude tracks with $b_0 k_{y\text{max}} / |\nabla r|_0$ as shown in Fig. 5. The best fit between the width of the zonal potential spectrum and $b_0 k_{y\text{max}} / |\nabla r|_0$ is $b_0=0.75$ for the κ scan and $b_0=0.9$ for the Δ scan. There is a lot of variation in the quality of the Lorentzian fit to the zonal potential so these differences are probably not significant. The best fit to the GASTD case of $b_0 = 0.83$ used in Fig. 4 is within this range.

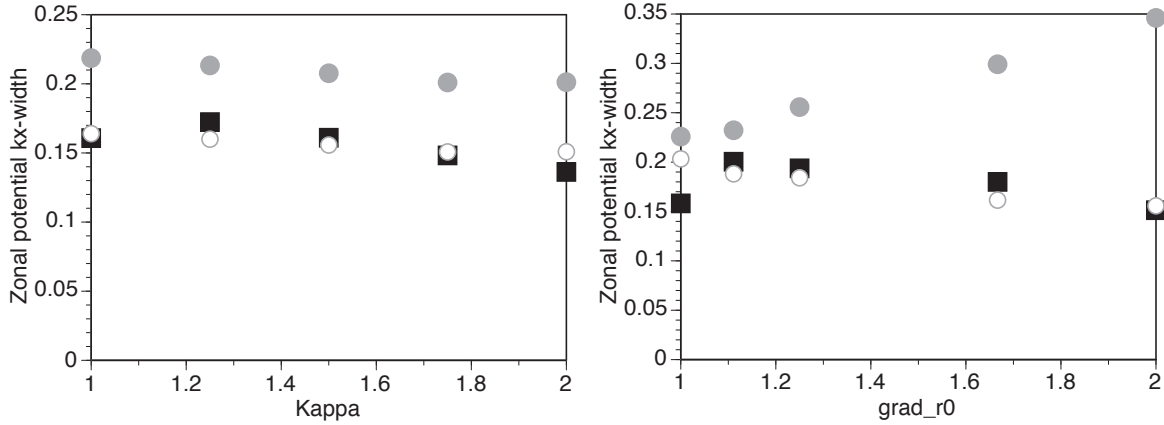


Figure 5. The zonal potential spectrum width k_x^{RMS} computed from the potential intensity at the outboard midplane (black, box) for (left) κ and (right) Δ scans also shown are the values of $k_{y\max}$ (gray, circles) and $b_0 k_{y\max} / |\nabla r|_0$ (open gray circles)

This model for k_x^{RMS} (Eq. 17) is an improvement at low- k_y over the original model (SAT1) in Ref. [5] that had $k_x^{\text{model}} = k_y$ in the ion range of $k_y < 1$. If the denominator of the model for the potential (Eq. 9) was chosen to be K_\perp^2 instead of $k_x^{\text{RMS}} k_y$, the width of the k_x spectrum at $\theta = 0$ would be $k_x^{\text{model}} = k_y G_q(0) / |\nabla r|_0$. This is similar to Eq. 17 for $k_y > k_{y\text{cut}}$ except for the extra factor of $|\nabla r|_0$. The Δ scan in Fig. 4 rules this factor out. Using K_\perp^2 in the model for the potential would also not reproduce the observed flattening of k_x^{RMS} at low k_y .

The effective non-linear growthrate γ^{eff} can be computed from the non-linear potential spectrum using the k_x^{RMS} determined by the spectrum in Eq. 11. As has been observed for many spectra, the effective growthrate is quite flat and independent of k_y above $k_{y\max}$, where the maximum in γ_{k_y} / k_y occurs, as shown in Fig. 6. The non-linear effective growthrate is well fit by the linear growthrate γ_{k_y} for $k_y < k_{y\max}$. For the GASTD case, the effective growthrate is well modeled by

$$\begin{aligned} \gamma_{k_y}^{\text{model}} &= b_2 \gamma_{k_y} \text{ for } k_y < k_{y\max} \\ &= b_2 \gamma_{\max} \text{ for } k_y \geq k_{y\max} \end{aligned} \quad (18)$$

Here γ_{\max} is the value of the linear growthrate at $k_{y\max}$. The best fit for the outboard midplane is $b_2 = 7.5$. This model (Eq. 18) is simpler than the original SAT1 model [5] since it does not have the subtraction of the zonal flow mixing term that was included in the original model for $k_y \leq k_{y\max}$. The new model (Eq. 18) is a better fit to $\gamma_{k_y}^{\text{eff}}$ (Fig. 6 (left)) in this range of k_y .

The slope of γ^{eff} with k_y changes with both κ and Δ away from the GASTD case. Using information from the next section on the poloidal dependence of the spectrum, a form factor $G(0)$ is proposed here to modify the model for γ^{eff} at the outboard midplane.

$$\begin{aligned} G(0) &= 1.0 \text{ for } k_y < k_{y\text{cut}} \\ &= \sqrt{(k_{y\text{cut}} + b_3(k_y - k_{y\text{cut}}) / G_q^2(0)) / k_y} \text{ for } k_y \geq k_{y\text{cut}} \end{aligned} \quad (19)$$

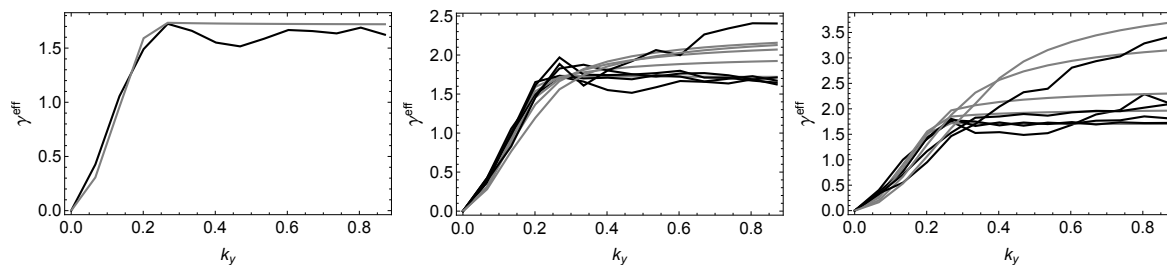


Figure 6. The $\gamma_{k_y}^{\text{eff}}$ spectrum computed from the potential at the outboard midplane (black) Eq. 11 and $G(0)\gamma_{k_y}^{\text{model}}$ (gray) for the GA-STD case (left) the κ scan (middle) and the Δ scan (right).

The $\gamma_{k_y}^{\text{eff}}$ computed from the potential spectrum and the model $G(0)\gamma_{k_y}^{\text{model}}$ are shown in Fig. 6 for $b_3 = 0.7$. The fit is not very tight. Without $G(0)$ all of the cases would be flat for $k_y > k_{y\text{max}}$. The geometric factor $G(0)$ does not appear to be required except for the highest range of $\kappa=2.0$ and $\Delta = -0.5$. These were run with a different collision frequency than the others and a smaller range of k_y and k_x . The GENE runs of these same cases show the same increase in slope. The need for the geometry factor $G(0)$ is better motivated by the poloidal dependence of the intensity as will be discussed in the next section.

4. Poloidal angular dependence of the 3D potential fluctuation intensity

In order to make a clear distinction in the poloidal angle dependence between the two geometric factors (B and $|\nabla r|$), CGYRO runs were done at $\kappa = 1.5$ and $\Delta = -0.25$ and $\text{RMIN}=0.8$, $\text{NU_EE}=0.05$ with the same poloidal and radial wavenumber resolutions as the 7 other CGYRO runs at this collision frequency. These choices make the magnetic field a broad function of θ and the factor $|\nabla r|$ a narrow function of θ that changes slope at $\theta = \pi$. Two cases with different magnetic shear $\hat{s} = 1.0, 0.5$ were run. The 2D intensity of potential fluctuations was saved at eight points: $\theta = -\pi, -3\pi/4, -\pi/2, -\pi/4, 0, \pi/4, \pi/2, 3\pi/4$. Where θ is the Miller geometry angle [7]. The ratio $\theta_x = k_x/(\hat{s}k_y)$ is a useful coordinate for plotting since it is involved in the ballooning space extension of θ . The θ_x -spectrum of the normalized potential amplitude Φ for $k_y = 0.25$, $\hat{s} = 1.0$ is plotted for the negative θ values in Fig. 7 (left). The positive θ spectra are essentially the mirror image of the negative ones about the $k_x = 0$ axis. From Fig. 7 it is clear that there is a peak at $k_x = 0$ and there is a skew towards the $-\theta$ direction. The case $\theta = -\pi$ on the right panel of Fig. 7 shows that there is an approximate reflection symmetry about the line $\theta_x = \pi$ with a second peak at $\theta_x = 2\pi$ with the same amplitude as the peak at $\theta_x = 0$. The value at $\theta_x = \pi$ is lower than the two peaks for $k_y < k_{y\text{min}}$ and is the dominant peak for $k_y > k_{y\text{min}}$ for $\theta = -\pi$. The symmetry of the spectrum at $\theta = -\pi$ can be understood from the quasi-periodicity of

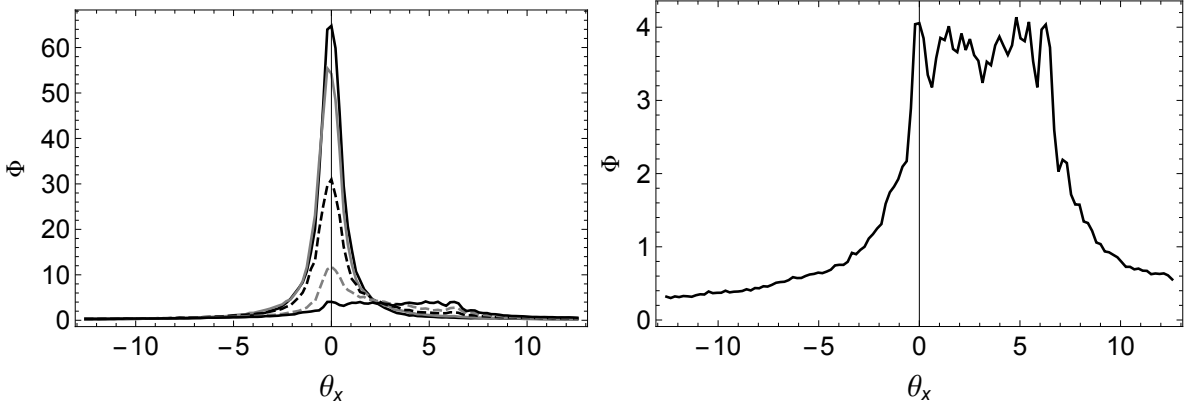


Figure 7. The $\theta_x = k_x/(\hat{s}k_y)$ spectrum of the normalized potential amplitude Φ for $k_y = 0.25$ and $\hat{s} = 1.0$ for $\theta = -\pi, -3\pi/4 - \pi/2, -\pi/4, 0$ (left) and just $\theta = -\pi$ (right)

the eikonal [3].

$$\tilde{\phi}(k_y, k_x, \theta) = \tilde{\phi}(k_y, k_x - 2\pi\hat{s}k_y, \theta + 2\pi) \quad (20)$$

Due to this quasi-periodicity property, the peak of the potential at $\theta = -\pi$ and $\theta_x = 2\pi$ in the right panel of Fig. 7 is the image of a peak at $\theta_x = 0, \theta = \pi$. The spectrum at $\theta = \pi$ would be the reflection of the plot in Fig. 7 (right) about the line $\theta_x = 0$. There are no peaks at larger values of $|\theta_x| > 2\pi$ so really there is only the peak at $\theta_x = 0$ and its images at $\theta_x = \pm 2\pi$ within the range of θ .

The 3D spectrum in the space k_y, k_x, θ is like a house of mirrors with internal reflections due to the dual nature of k_x both as a Fourier wavenumber for the radial coordinate and as the enforcer of the quasi-periodicity property. The potential spectrum can be mapped onto an extended ballooning angle coordinate θ_b . This coordinate extends the range of $-\pi \leq \theta \leq \pi$ by adding a translation in θ_x by 2π at the boundary of each circuit of θ . This continues for each θ circuit until the limit of the range of θ_x is reached. The independent ballooning modes can be labeled by $k_{x0} = \ell dk_x = \ell \hat{s} dk_y 2\pi / N_{\text{box}}$ with the integer ℓ having the range $-(N_{\text{box}} - 1) \leq \ell \leq (N_{\text{box}} - 1)$. For the case $\hat{s} = 1.0$ there are 11 k_{x0} 's ($N_{\text{box}} = 6$). The quasi-periodicity property Eq. 20 can be used to map the potential onto the ballooning mode space for each independent ballooning mode. The result is shown in Fig. 8 for $k_y = 0.25, \hat{s} = 1$. The highest peak is for $\ell = 0$, the next highest pair $\ell = \pm 1$ etc. down to the lowest amplitude pair $\ell = \pm 5$. Most of the amplitude of all of the ballooning modes is within the original range ($\pm\pi$) of θ . The width of all of the ballooning modes is mostly contained in the envelope of the $\ell = 0$ mode.

The θ dependence of the potential at $k_x = 0$ is the same in the original theta space and in ballooning space within the first panel. The theta dependence of the intensity at $k_x = 0$ for all of the k_y 's is shown in Fig. 9. The intensity has been normalized to the intensity at $\theta = 0$. The left panel shows the range $0 \leq k_y \leq 0.55$. For this case $k_{y\text{max}} = 0.246$ so it is within this range. The zonal intensity $k_y = 0$ uses the peak of the fitted Lorentzian shown in Fig. 3. It is almost independent of θ . This is representative

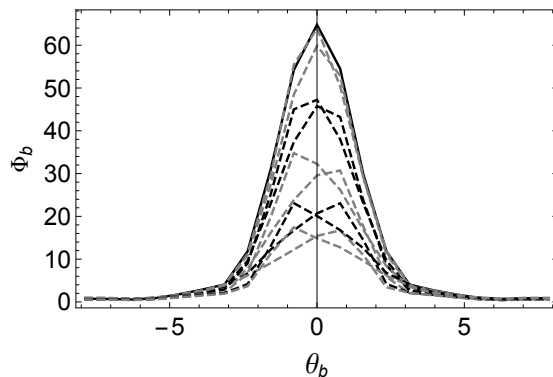


Figure 8. The ballooning angle θ_b dependence of the amplitude of the potential Φ_b for the 11 independent ballooning modes of the CGYRO spectrum for $k_y = 0.25$

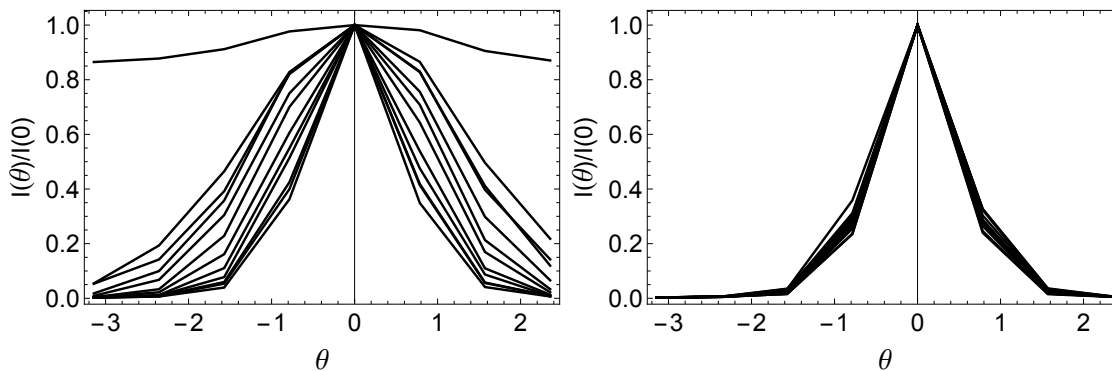


Figure 9. The intensity for $k_x = 0$ normalized to $\theta = 0$ for (left) $0 \leq k_y \leq 0.55$ and (right) $0.55 < k_y \leq 1.15$

of the whole zonal k_x -spectrum that is remarkably independent of poloidal angle. The shape becomes progressively narrower for increasing k_y until it saturates. The right plot in Fig. 9 has all of the other values $0.55 < k_y \leq 1.15$. The shape of the intensity is the same for all these values. It is not hard to imagine that this result could be due to the non-linear convolution of the zonal potential with the finite k_y potential causing a broadening of the θ dependence at low k_y along with the broadening of the k_x^{RMS} width. However, the shapes for $k_y = 0.05, 0.1, 0.15$ are nearly the same rather than broadening towards $k_y = 0$.

Two geometric shape functions have been found that fit the two ends of the k_y spectrum.

$$G_1 = \left(\frac{B(0)}{B(\theta)} \right)^4 \quad (21)$$

$$G_2 = \left(\frac{B(0)}{B(\theta)} \right)^4 \left(\frac{|\nabla r|}{|\nabla r|_0} \right)^4 = \left(\frac{G_q(0)}{G_q(\theta)} \right)^4 \quad (22)$$

These two shape functions are shown in Fig. 10. The magnetic field shape function (G_1) (gray) is broader and fits the low $k_y = 0.1$ intensity shape (black) very well as shown in the left plot. The shape function G_2 has the factor G_q that appears in the model for the

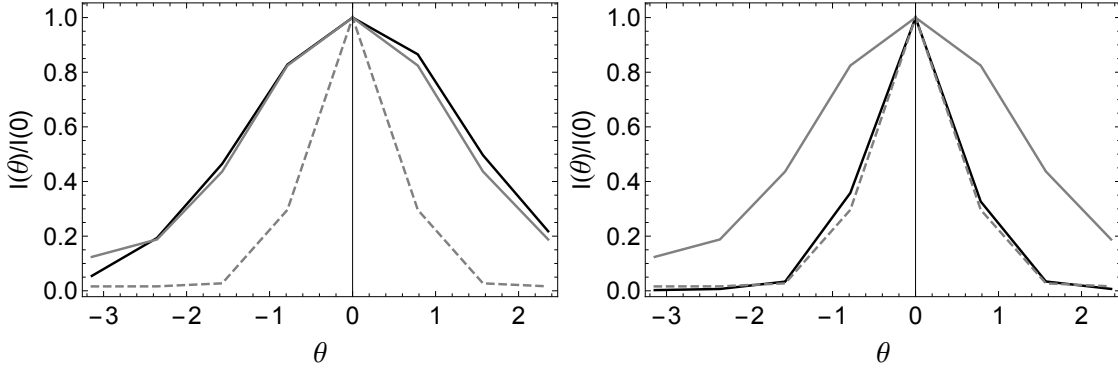


Figure 10. The intensity for $k_x = 0$ normalized to $\theta = 0$ (black) for $k_y = 0.1$ (left) and $k_y = 0.65$ (right) and two shape functions G_1 (grey) and G_2 (grey dashed)

k_x^{RMS} (Eq. 17) but raised to the fourth power. These shape factors are normalized to the outboard miplane value like the intensities in Fig. 10. The second shape factor (gray dashed) is a very good fit to the higher k_y spectrum (black) shown in the right panel of Fig. 10. These two shape functions will be used in the next section to build a model that interpolates between them to cover all k_y . A CGYRO simulation was run for the same case but with magnetic shear of $\hat{s} = 0.5$. This was run to see if the shape changes with magnetic shear. The two shape functions G_1 and G_2 do not depend upon shear but the perpendicular wave vector K_{\perp}^2 evaluated at $k_x = 0$ does. It was found that the shape at $\hat{s} = 0.5$, at low and high k_y , was the same as for $\hat{s} = 1.0$. The perpendicular wave vector would give a shape function that was independent of k_y and broader for $\hat{s} = 0.5$, so it cannot reproduce the observed non-linear intensity spectrum. Once again, this rules out the use of K_{\perp}^2 as the denominator of the model of the potential spectrum.

Similarly, the lack of magnetic shear dependence also rules out the following extension of the Lorentzian model to fit the $\theta = 0$ spectrum:

$$1/\left(1 + \left(\frac{\hat{s}k_y\theta}{k_x^{\text{RMS}}}\right)^2\right)^2 \quad (23)$$

This shape function comes from assuming that k_x in Eq. 16 is replaced by $k_x + \hat{s}k_y\theta$ in general and then taking $k_x = 0$ to get Eq. 23. The difference between θ and Θ in Eq. 4 is not important for this argument. The problem with the shape function Eq. 23 is that the k_x^{RMS} computed by fitting the spectrum at $\theta = 0$ does not depend on magnetic shear \hat{s} and neither does the shape in θ of the non-linear potential spectrum Fig. 9.

The shape function G_1 could be replaced by the Gaussian envelope of the linear eigenmodes. This is appealing, and can give a good fit to the low k_y spectrum. However, as we will see in the next section, when you include the peak amplitude of the potential in the fit to the QL intensity, G_1 is un-modified but G_2 is replaced by $(G_q(\theta))^{-4}$ for the best fit. Hence, G_1 is not a common factor of these two shape functions in the final analysis and it cannot be replaced by a Gaussian envelope in both shape functions as would be the case if it were from the wavefunction envelope.

Note that the flux surface average of the fluxes employed in the gyrokinetic codes

covers only the range of θ . It is the sum over k_x that includes the extended ballooning angle. The potential intensity is very small for $|\theta_x| \geq 2\pi$ so the ballooning mode extensions do not contribute much to the flux. The simplest interpretation, that the shape in θ of the potential intensity spectrum at $k_x = 0$ comes from the geometric factors in Eqs. 21, 22, holds up to this analysis of alternatives. It does not prove it is unique and should be tested on more cases.

5. A model of the intensity required for a quasi-linear flux calculation

Until now the 3D intensity of potential fluctuations has been examined in various ways to reveal the shape dependence. Now the ultimate goal of modeling the QL intensity required to compute the fluxes will be addressed. The QL intensity involves a flux surface average and a sum over k_x of the intensity weighted by the QL weight (cross-phases) of all of the modes in the non-linear spectrum. Only the QL weight of the most unstable mode was used to compute the QL intensity (Eq. 1). Each of the independent ballooning modes with different values of k_{x0} contribute to the flux in some way. Therefore, it is expected that the QL intensity is not just the flux surface average of the 3D intensity evaluated at $k_x = 0$ or summed over k_x without the QL weights of the non-zero k_{x0} ballooning modes. This is easily shown by comparing the QL weight computed from the spectrum with these two proxy candidates. This is a distraction from the goal of building a model of the QL intensity directly from the linear CGYRO eigenvalue spectrum so it will not be presented here. Models for k_x^{model} (Eq. 17 and $\gamma_{k_y}^{\text{model}}$ (Eq. 18) have already been found and can provide a useful template for the final construction. The model template is

$$I_{k_y}^{\text{model}} = \left\langle G^2(\theta) \right\rangle_{\theta} \left(\frac{\gamma_{k_y}^{\text{model}}}{k_x^{\text{model}} k_y} \right)^2 \quad (24)$$

For simplicity, all of the θ dependence is absorbed into $G(\theta)$

$$\begin{aligned} G^2(\theta) &= d_1 G_1(\theta) \text{ for } k_y < k_{\text{ycut}} \\ &= \left(d_1 G_1(\theta) k_{\text{ycut}} + b_3 d_2 G_2(\theta) (k_y - k_{\text{ycut}}) \right) / k_y \text{ for } k_y \geq k_{\text{ycut}} \end{aligned} \quad (25)$$

where the best fit for the coefficients d_1, d_2 is found to be

$$d_1 = 1/(|\nabla r|_0)^2 \quad (26)$$

$$d_2 = 1/G_q(0)^2 \quad (27)$$

The model k_x^{model} was fit to the outboard midplane k_x^{RMS} . This leaves it ambiguous if the geometric factors become functions of θ in general. The best fit coefficient d_1 (Eq. 26) cancels the geometric factor $|\nabla r|_0$ from k_x^{model} for $k_y < k_{\text{ycut}}$. This is why it is important for G^2 to have the same k_{ycut} as k_x^{model} . For $k_y \geq k_{\text{ycut}}$, the factor $G_q(0)$ in k_x^{model} does

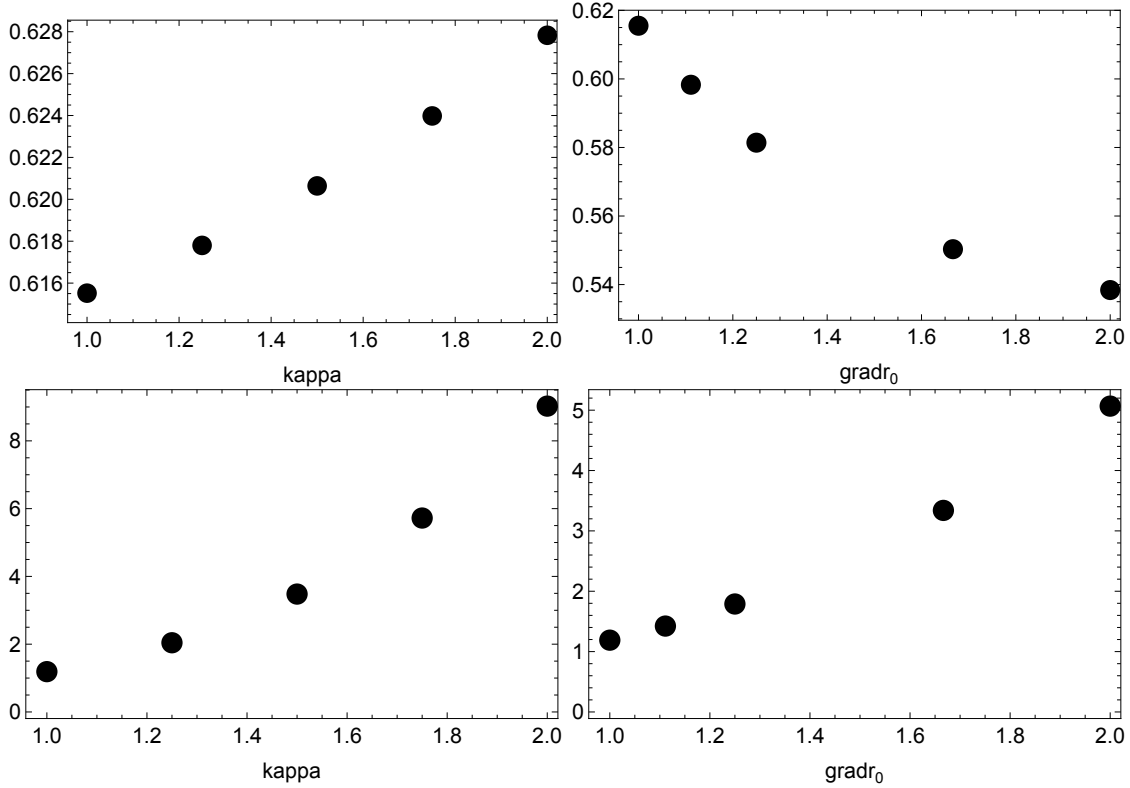


Figure 11. The flux surface averages \hat{G}_1 (top) and \hat{G}_2 (bottom) for the κ (left) and $\text{gradr}_0 = 1/(1+\Delta)$ (right) scans

get promoted to its θ dependent form. This contributes two powers to G_2 . The other two powers are needed to fit $\gamma_{k_y}^{\text{eff}}$ (Eq. 19). The best fit for the coefficient d_2 (Eq. 27), changes $d_2 G_2 / (k_x^{\text{model}} k_y)^2$ to the shape factor $(G_q(\theta) k_y)^{-4}$ for $k_y \gg k_{y\text{max}}$. Since $G^2(\theta)$ is linear in G_1 and G_2 the flux surface average of these terms can be computed separately and then used in the formula for the intensity model Eq. 24.

To see how these weight the model for the QL intensity, the flux surface averages $\hat{G}_1 = \langle G_1 \rangle_\theta$ and $\hat{G}_2 = \langle G_q^{-4} \rangle_\theta$ are plotted in Fig. 11 for the κ and Δ scans. The flux surface average \hat{G}_1 (top plots) is weakly varying. It has an influence on the slope of the very low $k_y < k_{y\text{max}}$ part of the spectrum and the peak value of the QL intensity model plotted in Fig. 12. The flux surface average \hat{G}_2 (bottom plots of Fig. 11) has a strong variation with both κ and Δ (gradr_0). This is primarily due to the variation of $G_q^{-4}(0)$. The \hat{G}_2 factor impacts the way the intensity falls off with k_y for $k_y \gg k_{y\text{max}}$. The effect can be clearly seen in Fig. 12. The QL intensity spectrum, computed from the CGYRO Q_e , (black) is much broader for the $\kappa = 2.0$ (center) and $\text{gradr}_0 = 2.0$ (i.e. $\Delta = -0.5$) (right) than the GASTD case (left). All of these cases are with the same collision frequency (0.1). The broadening for the Δ scan is partly due to the higher k_y of the peak due to $k_{y\text{max}}$ as seen in Fig. 5. The value of the geometry factor \hat{G}_2 is largest for $\kappa=2.0$ and its effect on the spectrum is important for the accuracy of the fluxes and the overall scaling of the fluxes with κ and gradr_0 .

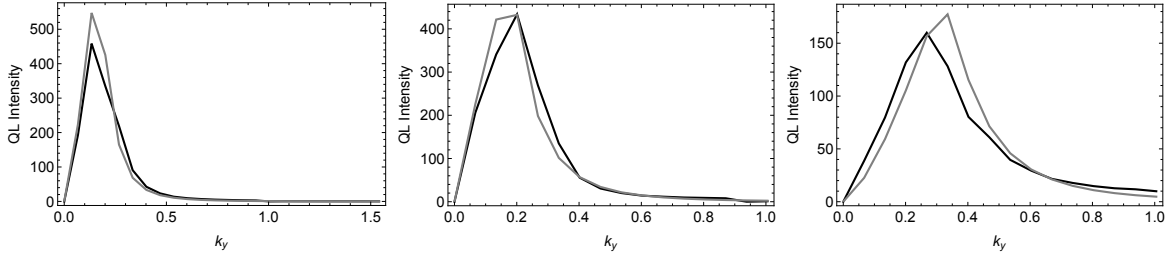


Figure 12. The QL intensity (black) and the optimum fit model (gray) Eq. 24 for GASTD (left), $\kappa = 2.0$ (middle) and $\Delta = -0.5$ (right) all with collision frequency 0.1

There are four fitting coefficients in the model template (Eq. 24) b_0, b_1, b_2, b_3 . The coefficient b_2 from $\gamma_{k_y}^{\text{model}}$ (Eq. 18) acts as an overall multiplier. It will be determined by setting the net offset of the model fluxes and the CGYRO fluxes for the ten cases (scans in κ and Δ) to zero. The other three coefficients will be adjusted to find the minimum RMS error between the model and CGYRO for the per k_y flux contributions. There are 10 CGYRO runs and 14 k_y 's included in the RMS error for both electron and ion fluxes for a total of 280 data points being fit. The optimum coefficients were found to be $b_0 = 0.72$ for $k_{y\text{cut}}$, $b_1 = 1.22$ for the slope of k_x^{model} , $b_3 = 0.88$ for the slope of G^2 and $b_2 = 4.93$ for the zero offset condition. These values give an RMS error average of 0.55 GB units for each k_y flux contribution. The error for the total fluxes for the whole set of 10 cases are 4.4% for Q_e and 5.2% for Q_i . The total fluxes for each scan are shown in Fig. 13. The overall trend of the fluxes with κ and gradr0 is very well matched. Recall that the $\kappa=2.0$, $\text{gradr0}=1.0$, 2.0 CGYRO runs were done with a higher collision frequency (0.1) than the others (0.05) which lowers the fluxes for these points. The overall scaling trend is approximately $Q \propto 1/G_q(0)$. This optimum fit is a fairly broad minimum. Using the values found from the fits to the spectra at $\theta = 0$: $b_0 = 0.83$, $b_1 = 1.31$, $b_3 = 0.7$ with the offset zero constraint giving $b_2 = 5.59$ is not much different. The total flux errors are 6.4% for Q_e and 4.0% for Q_i .

The result of computing the SAT1 model fluxes [5] using the CGYRO linear eigenmode spectrum is also shown in Fig 13 as small gray dots. The trend of the fluxes is flat or downward for both scans. The SAT1 model does not have any explicit geometric terms. It is effectively assuming that B_{unit} is the natural magnetic field that sets the local turbulence gyro-radius and eddy size. This model was calibrated to a set of 83 GYRO [11] simulations that included κ scans but not Δ scans. The simulation database was assembled 15 years ago in order to calibrate the original (SAT0) TGLF transport model [12]. Low poloidal and radial grid resolutions were used in order to speed up the simulations. GYRO uses a grid in the minor radius so that it can run both periodic and non-periodic (global) gyrokinetic simulations. It can compute gyro-averages with spectral accuracy (like CGYRO) using an exact Bessel function expansion, but this is expensive and was not done for these runs. The trend with κ for these low-resolution GYRO runs agrees with the SAT1 model fluxes in Fig. 13. This is a lesson learned. A model is no more accurate than the simulations it fits. It also is a caution

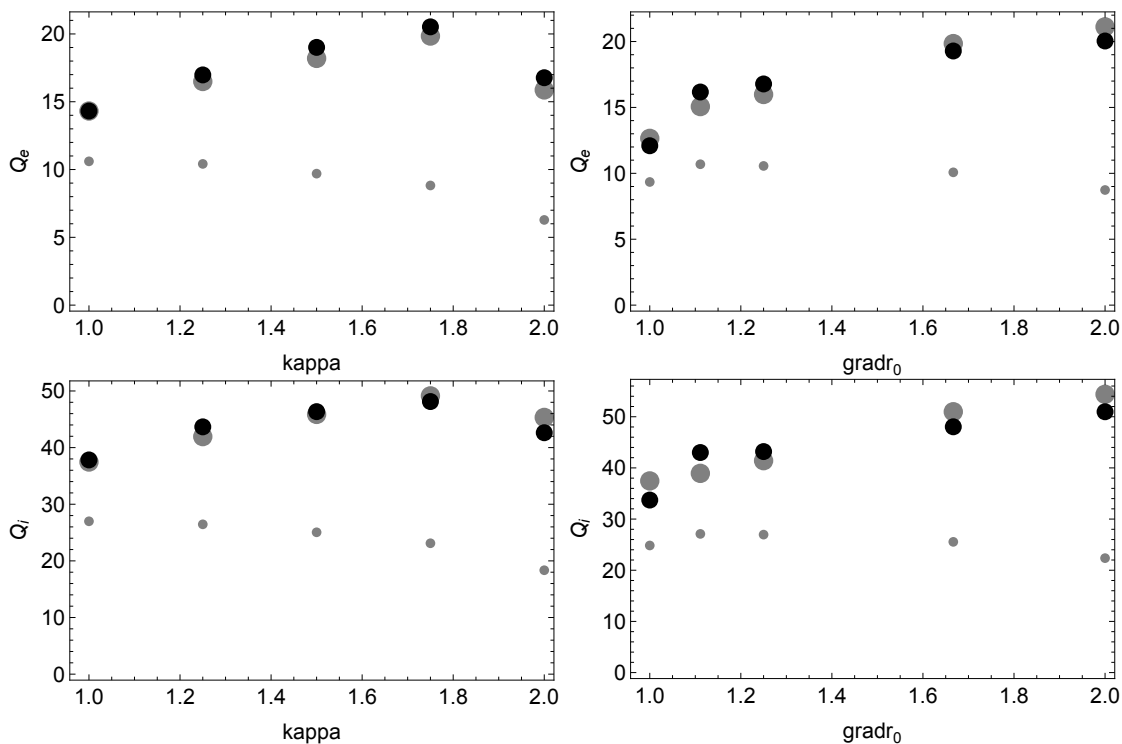


Figure 13. The total electron (top) and ion (bottom) energy fluxes for a κ scan (left) and a $\text{grad}r_0 = 1/(1+\Delta)$ scan (right) for CGYRO (black), optimum model (large gray) and the original SAT1 model (small gray)

to present day attempts to run reduced physics fidelity global simulations in order to capture long range wave-like effects. The reduced simulation models may not capture important local physics effects, like the geometric effects in this paper, that require accurate gyro-averaging (i.e. Bessel functions).

6. Summary

This paper presented the most accurate model of the flux spectrum ever developed for quasi-linear modeling. It is as accurate as the agreement between different gyrokinetic codes. It will not be as accurate on a larger set of gyrokinetic runs as it is for the 10 runs it was calibrated to. The four fitting coefficients may turn out to be functions of parameters that were not varied in these scans. Indeed, it will be shown in a separate paper, that in order to fit a much wider database of CGYRO runs, the overall coefficient b_2 needs to be generalized. However, the poloidal wavenumber (k_y) dependent geometry factor (Eq. 25) and the models for the radial wavenumber spectral width (Eq. 17), and the effective growth rate (Eq. 18) presented in this paper do not need to be changed in order to give a good fit to the larger database. The spectral shift model for $E \times B$ shear [10] and the electron scale turbulence [5] will also be re-calibrated in the separate paper. Previous experience with quasi-linear models leads to the expectation that the new

model will have sufficient accuracy for modeling the core transport of tokamaks under normal conditions. Preliminary test of TGLF with the fluxes multiplied by the overall scale factor $1/G_q(0)$ has been found to greatly improve the transport predictions for the edge region of L-modes for DIII-D and AUG plasmas. The prediction of transport in low aspect ratio spherical tori, which have strongly varying shape factors, should also be improved with the SAT2 model. This paper lays out new methodologies, like fitting to the QL intensity and 3D potential intensity. By computing the linear spectrum, and quasi-linear weights, with the same gyrokinetic code as the simulations, the process of modeling the QL intensity can be separated from the process of developing a fast reduced linear eigensolver by this approach.

The role of zonal flow mixing on setting the width of the k_x -spectrum for the finite k_y modes was explored in this paper. It was shown for the first time that the width of the zonal potential spectrum provides an irreducible minimum width. It was also shown that this width is coupled to the value of $k_{y\max}$ that also plays a role in setting the saturated RMS velocity of the zonal fluctuations through balancing the zonal flow mixing rate with the linear growthrate γ_{\max} (Eq. 14). This saturation rule for the zonal flow velocity was found to be independent of geometry. The width of the k_x -spectrum has a dependence on geometry (Eq. 17). For large k_x , this is consistent with the Bessel functions depending on K_x (Eq. 6). The argument of the Bessel function has the physical total magnetic field gyro-radius normalizing the radial wavenumber. Hence the radial correlation length at the outboard midplane scales with the local total magnetic field. At low k_x the influence of the zonal flow mixing takes over and the poloidal wavenumber argument of the Bessel function (Eq. 5) sets the geometry dependence. The form of Eq. 5 shows that the toroidal correlation length scales with the poloidal magnetic field gyroradius. The new model for k_x^{RMS} (Eq. 17) is an improvement over the SAT1 model.

The model for the effective non-linear growthrate $\gamma_{k_y}^{\text{eff}}$ at low- k_y was also improved in this paper (Eq. 18). It was found that there was no need for the zonal flow mixing subtraction used in the SAT1 model below the peak at $k_{y\max}$. This is because the flattening of k_x^{RMS} at low k_y , due to the zonal potential setting a minimum width, suppresses the transport at low k_y enough. No additional suppression is required in the model. This change to the model improves the fit to the QL intensity at low k_y significantly. An overall geometric factor was found to be needed in order to match the change in slope of $\gamma_{k_y}^{\text{eff}}$ at high k_y with flux surface shape. This shape factor is consistent with the findings of the poloidal dependence of the peak intensity at $k_x = 0$.

Perhaps the most controversial part of the analysis of the 3D spectrum in this paper is the finding that the poloidal dependence of the peak of the intensity spectrum at $k_x = 0$ can be fit with purely geometric factors. This conclusion is based on only two cases ($\hat{s} = 1.0, 0.05$) so it will need further verification. Clearly, the geometric factors fit the spectra in Fig. 10 for the cases tested, but it was expected that some dependence on the shape of the most unstable linear eigenmode wavefunction would be found. It is interesting that the linear eigenmodes found with TGLF have a Gaussian envelope that is not far from the shape of $(B(0)/B)^2$ at low- k_y . The wavefunction envelope becomes

narrower at higher k_y . It may be that this is caused by the same geometric factors entering the linear TGLF equations (velocity moments of the gyrokinetic equations). The non-linear turbulence spectrum includes all modes, not just the most unstable one, so the wavefunction shape may become washed out in the non-linear simulation but the quasi-linear weight, that depends on the eigenmode frequency, is still preserved by the turbulence. Further study is required to follow up on these questions.

7. Acknowledgements

Discussions with J. Citrin, P. Mantica R. Waltz and H. Dudding contributed to this work. This work was supported by the U.S. Department of Energy under DE-SC0019736, DE-SC0018990, DE-FG02-95ER54309, and DE-FC02-04ER54698. We acknowledge the CINECA award under the ISCRA initiative, for the availability of high performance computing resources and support. This work has been carried out within the framework of the EUROfusion Consortium and has received funding from the Euratom research and training programme 2014-2018 and 2019-2020 under grant agreement No 633053. The views and opinions expressed herein do not necessarily reflect those of the European Commission. This work was supported by the Engineering and Physical Sciences Research Council [EP/L01663X/1].

Disclaimer-This report was prepared as an account of work sponsored by an agency of the United States Government. Neither the United States Government nor any agency thereof, nor any of their employees, makes any warranty, express or implied, or assumes any legal liability or responsibility for the accuracy, completeness, or usefulness of any information, apparatus, product, or process disclosed, or represents that its use would not infringe privately owned rights. Reference herein to any specific commercial product, process, or service by trade name, trademark, manufacturer, or otherwise, does not necessarily constitute or imply its endorsement, recommendation, or favoring by the United States Government or any agency thereof. The views and opinions of authors expressed herein do not necessarily state or reflect those of the United States Government or any agency thereof.

References

- [1] R.E. Waltz, G.M. Staebler, W. Dorland, G.W. Hammett, M. Kotschenreuther, and J.A. Konings. A gyro-landau fluid transport model. *Phys. Plasmas*, 4:2482, 1997.
- [2] G.M. Staebler, J.E. Kinsey, and R.E. Waltz. Gyro-landau fluid equations for trapped and passing particles. *Phys. Plasmas*, 12:102508, 2005.
- [3] J. Candy, E.A. Belli, and R.V. Bravenec. A high-accuracy eulerian gyrokinetic solver for collisional plasmas. *Journal of Computational Physics*, 324:73 – 93, 2016.
- [4] R.E. Waltz and R.L. Miller. Ion temperature gradient turbulence simulations and plasma flux surface shape. *Phys. Plasmas*, 6:4265, 1999.
- [5] G.M. Staebler, J. Candy, N. T. Howard, and C. Holland. The role of zonal flows in the saturation of multi-scale gyrokinetic turbulence. *Phys. Plasmas*, 23:062518, 2016.

- [6] N. T. Howard, A. E. White, M. Greenwald, C. Holland, and J. Candy. Multi-scale gyrokinetic simulation of Alcator C-Mod tokamak discharges. *Phys. Plasmas*, 21:032308, 2014.
- [7] R.L. Miller, M.S. Chu, J.M. Greene, Y.R. Lin-liu, and R.E. Waltz. Non-circular, finite aspect ratio, local equilibrium model. *pop*, 5:973, 1998.
- [8] F. Jenko, W. Dorland, M. Kotschenreuther, and B.N. Rogers. Electron temperature gradient driven turbulence. *Phys. Plasmas*, 7:1904, 2000.
- [9] P. Xanthopoulos and F. Jenko. Clebsch-type coordinates for nonlinear gyrokinetics in generic toroidal configurations. *Physics of Plasmas*, 13(9):092301, 2006.
- [10] G.M. Staebler, R.E. Waltz, J. Candy, and J.E. Kinsey. A new paradigm for suppression of gyrokinetic turbulence by velocity shear. *Phys. Rev. Lett.*, 110:055003, 2013.
- [11] J. Candy and R.E. Waltz. An Eulerian gyrokinetic-Maxwell solver. *J. Comput. Phys.*, 186:545, 2003.
- [12] J.E. Kinsey, G.M. Staebler, and R.E. Waltz. The first transport code simulations using the trapped gyro-landau-fluid model. *Phys. Plasmas*, 15:055908, 2008.